RSC Applied Interfaces

ROYAL SOCIETY OF CHEMISTRY

PAPER

View Article Online
View Journal | View Issue

Cite this: *RSC Appl. Interfaces*, 2025, 2, 1661

Unraveling clogging of solid-state nanopores by selective polymer coating: surface potential measurements and sensing of long single stranded DNA

Mohamed Yassine Bouhamidi, [ab]
Zachary Roelen [a] and Vincent Tabard-Cossa *[ab]

Solid-state nanopores have emerged as powerful tools for single-molecule analysis, with applications ranging from genomics to diagnostics. However, challenges such as surface interactions and clogging have limited their applicability, and a better characterization of the nanopore wall surfaces and control of the surface coating would provide valuable information to tackle these problems. Here, employing a platform capable of high-pressure streaming current measurements in the picoampere range, we characterize the surface potential of solid-state nanopores and perform selective surface coating to elucidate the mechanism for molecular clogging. By examining different operating conditions, such as pore diameter, salt concentration, and pH, we discuss optimizations for precise streaming current measurements. We validate the performance of the setup by studying both bare SiN and polymer-coated nanopores fabricated by the controlled breakdown method. To address the issue of nanopore clogging, we investigate localized functionalization approaches either prior to or after pore formation. Our results allow us to establish that outer membrane coating is sufficient to provide antifouling properties during translocation of long single-stranded DNA, and provide insight into the mechanism of nanopore clogging.

Received 21st May 2025,
Accepted 5th August 2025

DOI: 10.1039/d5lf00147a

rsc.li/RSCApplInter

Introduction

Nanopores are small holes in thin insulating membranes used to analyze single molecules such as DNA, RNA, and proteins.[1–3] When immersed in a salt solution, these molecular-sized channels produce an ionic current in response to a voltage gradient. The passage of charged analytes by electrophoresis through the pore, one at a time, causes variations in this electrical signal. The resulting current blockages can provide critical information about the molecule's structure and composition.[4]

Nanopores, made in solid-state materials, such as SiN, offer a versatile platform for different biosensing applications by allowing for the tuning of the pore size to match the analyte. Recent advances in the controlled breakdown (CBD) method of nanopore fabrication have democratized access to solid-state nanopores of the desired size from 2 to 20 nm and expanded their field of use.[5,6] Yet, despite this technological progress, typical surface properties (such as roughness, charge density, precise pore shape and surface coating) of solid-state nanopores present significant challenges.

A major factor limiting the sensing performance of solid-state nanopores is the level of $1/f$ noise[7–10] in the ionic current signal (dominating up to 1 kHz), which has been linked to surface charges, as well as to the roughness and hydrophobicity of the nanopore membrane, factors which can promote nanobubble formation and trapping.[11–13] Furthermore, the levels of electrical interference arising from the protonation of the surface are greatly impacted by the working conditions of salt concentration and pH, and also lead to an increase in white noise (present at all frequencies).[14] Typically, surface charge density is determined experimentally using the streaming potential method[15] or is estimated theoretically through the expected degree of dissociation of silanol and amine groups.[16] Here, the streaming potential technique is favored for direct surface potential measurements, since the pressure actuation across the nanopore directly probes the motion of ions near the nanopore wall, neglecting the contribution from the bulk.

Surface interactions between the molecule and the pore also directly affect the sensing duration of an experiment,

[a] *Department of Physics, University of Ottawa, Ottawa K1N 6N5, Canada. E-mail: tcossa@uottawa.ca*
[b] *Ottawa-Carleton Institute of Biomedical Engineering, University of Ottawa, Ottawa K1N 6N5, Canada*

which usually terminates due to an irreversible clog where the nanopore's conductance is irrevocably reduced despite repeated voltage reversal. Mitigating clogging issues has been the subject of on-going studies of solid-state pores.[17–21] Techniques to promote nanopore anti-fouling properties have included location-agnostic functionalization of the SiN surface *via* silanization of carboxylic acid and polyethylene glycol (PEG),[22,23] grafted PEG brushes,[24] photohydrosilylation of acidic, basic and nonionizable end groups,[25] or coating with a fluid lipid bilayer.[26,27] While localized functionalization has been studied in anodic aluminum oxide nanoporous membranes, where inner and outer wall chemical modification enable a wide range of properties such as anti-interference, signal enhancement and ion gating,[28] a localized approach to chemical modification has yet to be studied in SiN and at the single-nanopore level. Addressing these challenges related to surface properties requires careful characterization of the surface charge density of bare and functionalized surfaces to control the quality of the surface coating and relate it to observations of improved sensing performance.

To shine some light into the clogging issue, optical observation of molecules has been performed over the years to provide additional information beyond the traditional electrical channel. Dual optical–electrical platforms were developed to add parallelization and specificity to the nanopore measurements.[29–31] Of interest to this work are fluorescence studies that tracked the capture and passage of molecules through nanopores to gain a better understanding of the transport process.[32] Indeed, an optical microscope-nanopore platform can provide relevant spatial information about the molecule leading up to the translocation through the pore, whereas the electrical signal is most sensitive when the molecule is inside the pore. By labeling DNA strands with fluorescent dyes, a spatial resolution of ~1 μm has been achieved by confocal laser scanning microscopy.[17–19] Meanwhile, through stimulated emission depletion (STED) super-resolution microscopy, the observation of the capture region around a nanopore with a ~100 nm resolution was achieved.[33] However, while these optical measurements offer advantages in terms of spatial resolution outside the pore, the temporal resolution is limited by the frame rate of the camera, offering snapshots of the molecule in the millisecond range, much slower than the translocation timescale through the pore, typically in the microsecond range. Details of the transport process and mechanisms of clogging are thus not well resolved optically.

In this work, we performed streaming current measurements using a modified version of our previously developed platform,[34] to investigate the effect of parameters such as salt concentration, pH, and pore diameter on the surface potential of SiN nanopores. Unlike traditional nanopore measurements in which a voltage is applied across the membrane,[35] streaming currents measurements are driven by applying a transmembrane pressure gradient. Similarly to electroosmosis, the streaming current is a result of the motion of excess ions in the electric double layer (EDL) shielding the charges on the nanopore wall. We show that the isoelectric point of SiN pores from the batch of chips used and fabricated by CBD is approximately 4.4, agreeing with the values previously observed ranging from ~4–5.[36,37] Finally, we propose a protocol for the selective coating (interior–exterior) of CBD-fabricated nanopores and compare the zeta potential of functionalized nanopores to that of bare SiN surfaces. In particular, by studying the translocation of 7 kilo-nucleotide (knt) single-stranded DNA (ssDNA), we show that coating only the surrounding membrane surface with an antifouling polymer, while leaving the nanopore walls unfunctionalized, is enough to impart significant improvements in sensing times, and in the number of translocated molecules during nanopore experiments.

Results & discussion

Platform for nanopore fabrication, characterization, and functionalization

Solid-state nanopores made in 20 nm thick SiN by the controlled breakdown method[6] were used in this study. To enable high-precision zeta potential measurements of the pore surface, we designed a pressure-driven system housed in a Faraday cage (Fig. 1(a)). Following system calibration, we applied pressure sweeps up to 0.3 MPa (in steps of 0.05 MPa), systematically recording the resulting streaming current for a duration of 30–120 seconds. The *trans* side of the nanopore was kept at atmospheric pressure as a reference, while the *cis* side was biased using a mechanical pressure regulator. These measurements formed the basis for extracting zeta potential and associated surface charge density values of nanopores under different operating conditions and surface treatments, which we explore in subsequent sections. To eliminate issues related to electrode potential drift when switching between solutions of different salt concentration and/or pH, a 40% PEGDa salt bridge[38,39] was used to decouple the Ag/AgCl electrodes from the sensing medium (*i.e.*, keeping them consistently immersed in reservoirs of 3 M KCl, pH 8). This improvement significantly reduced current drift in the 1–10 picoampere range that the streaming signals occupied, allowing for accurate measurements while also extending the electrode lifetime.

Fig. 1(b) depicts the principle of the streaming current that arises upon the application of a pressure difference across a nanopore due to the presence of surface charges on the pore wall. Fig. 1(c) shows a typical time trace of the streaming current, I_{stream}, generated under changes of transmembrane pressure gradient ΔP. These pressure gradient sweeps allow for the extraction of the pore interior zeta potential ζ. This metric characterizes the amount of net charge on the nanopore wall, as observed by an electrokinetic measurement such as the recording of streaming current. Under conditions of low or weak surface potentials in the Debye–Huckel regime, the zeta potential can be expressed as:[40]

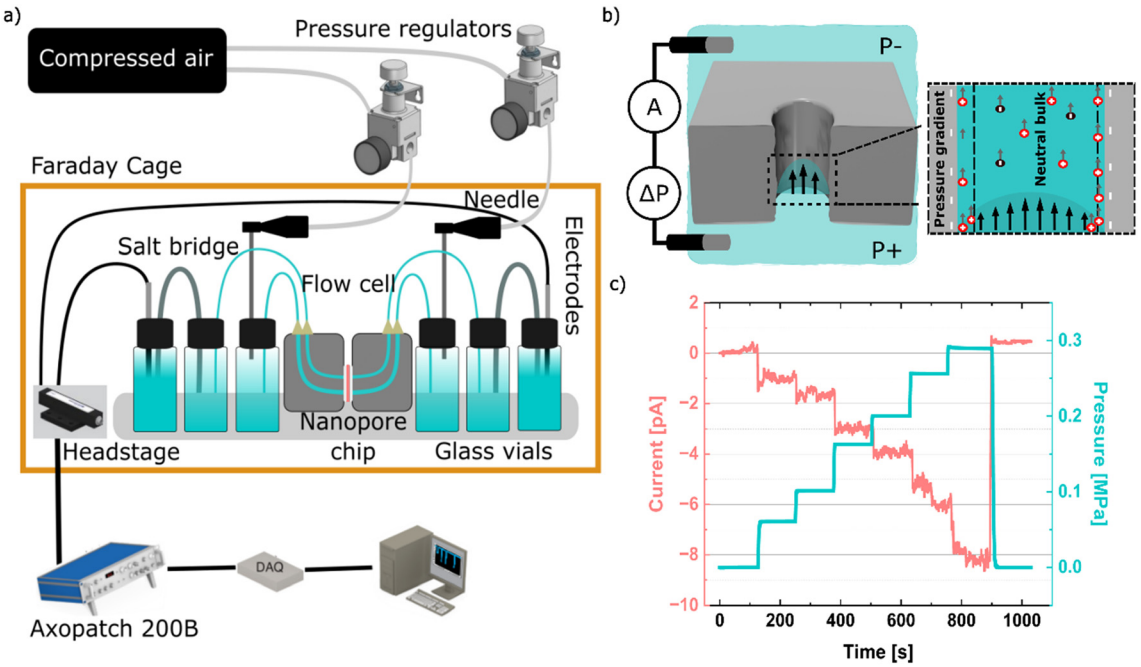

Fig. 1 Platform for fabrication, functionalization, and characterization of solid-state nanopores. a) System diagram depicting the different components of the voltage and pressure-controlled platform used to perform low-noise current measurements. b) Schematic highlighting the working principle of the streaming current method inside a nanopore. c) Typical I_{stream} (red) and ΔP (blue) curves *vs.* time for a streaming current measurement (10 nm SiN nanopore in 0.1 M KCl pH 8).

$$\zeta = \frac{\eta L \Delta I_{stream}}{\varepsilon_r A \Delta P} \quad (1)$$

in terms of the viscosity η and dielectric constant ε_r of the surrounding fluid (assumed uniform and in a laminar flow regime), the length L and cross-sectional area A of the nanopore, the applied pressure gradient ΔP (approximating that the pressure drop across the nanopore dominates over that of the access region, valid when $\sqrt{A} \lesssim L$), and measured streaming current I_{stream}.

By recording the streaming current under a sweep of pressure gradients, the zeta potential of the nanopore surface can be calculated from the slope of I_{stream} *vs.* ΔP using eqn (1), when $\lambda < d$ (where λ and d are the Debye length and nanopore diameter respectively). This approximation assumes the fact that the Hagen–Poiseuille law (laminar flow in a uniform circular channel) is respected for the nanopore with aspect ratios $d/L \sim 1$, used here.[41] The surface charge density, a property of the material interface with the solution, can also be estimated from the measured zeta potential using the Grahame equation for cylindrical nanopores:[16]

$$\sigma = \frac{2\varepsilon_r k_B T}{\lambda z e}\left[\sinh\left(\frac{ze\zeta}{2k_B T}\right) - \frac{2\lambda}{d}\tanh\left(\frac{ze\zeta}{4k_B T}\right)\right] \quad (2)$$

where z, e, k_B and T are the valence of ions, the elementary charge, the Boltzmann constant and the absolute temperature, respectively.

Here, we adopt the Debye length equation for monovalent salts at 25 °C as:

$$\lambda[\mathrm{nm}] = \frac{0.304}{\sqrt{C}} \quad (3)$$

where C is the salt concentration in units of mol L^{-1}. From eqn (1)–(3), we see how key experimental parameters—such as pore shape, salt concentration, and pH—can thus affect the surface charge density of a nanopore, through the Debye length and the streaming current observed.

Equipped with a setup for performing streaming current measurements, we next examined the effects of different operating parameters (pore size, salt concentration, and pH) on surface potential in order to optimize the measurement conditions. Fig. 2(a) plots the streaming current under a transmembrane pressure for three nanopores of varying diameters (10 to 25 nm) and identical nominal membrane thickness in 100 mM KCl pH 8, and shows a significant increase in streaming current magnitude with pore diameter. For example, at a fixed pressure gradient of 0.3 MPa, values of ~10 pA are observed for the 10 and 12 nm pores, compared to ~35 pA for the 25 nm diameter pore. We note that although the nanopore cross-sectional area A increases in the sequence of pore diameters tested, zeta potential calculations using eqn (1) for these nanopores give relatively consistent values of −7.3 ± 1.4, −7.0 ± 0.5 and −7.0 ± 0.3 mV for d = 10, 12 and 25 nm, respectively. The slight differences in extracted zeta potentials, being within the calculated standard deviations, lead us to conclude that the zeta potential stays constant for these nanopore dimensions (even for the case when $d > L$). On the other hand, the 4-fold increase in observed streaming current for the 25 nm pore

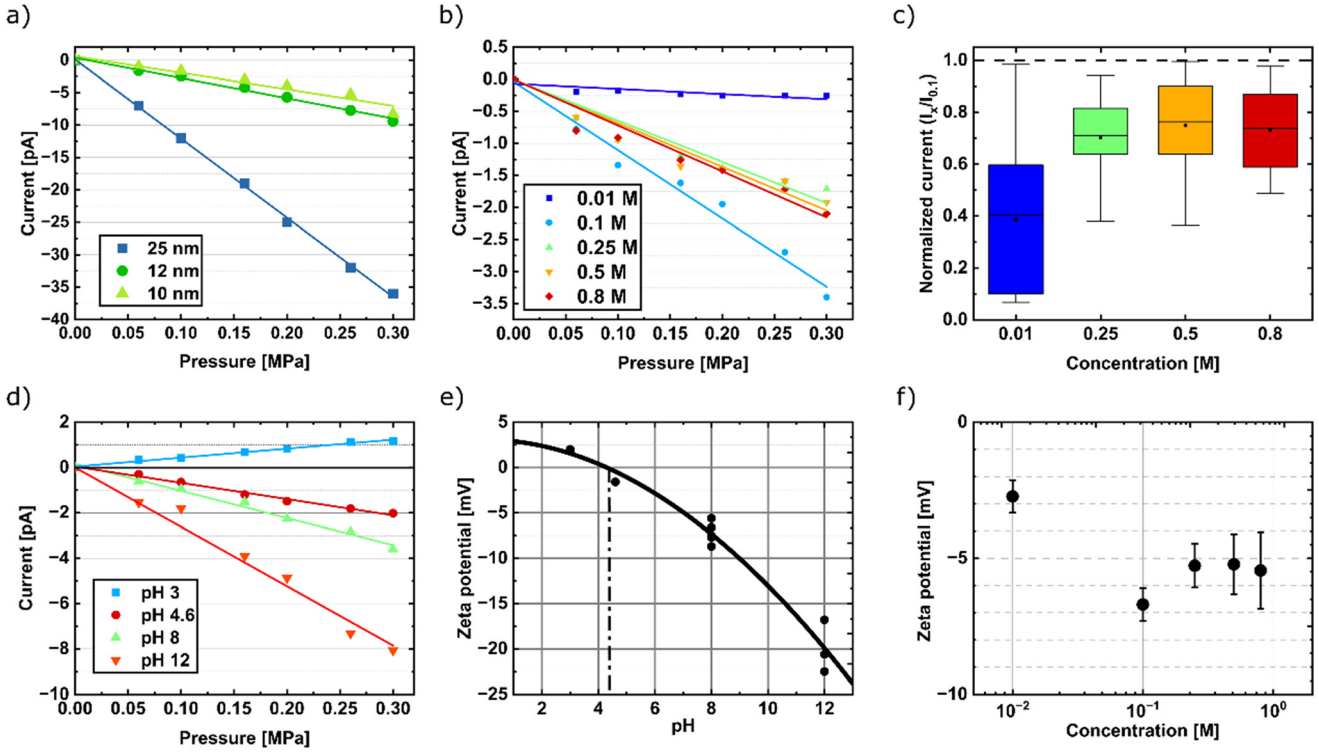

Fig. 2 Effect of SiN pore diameter, salt solution concentration and pH on zeta potential inside the nanopore. a) Streaming current measurements *versus* applied transmembrane pressure in 0.1 M KCl pH 8 for different nanopore diameters. b) Streaming current *versus* applied pressure gradient for a 9 nm nanopore in KCl solutions of different salt concentrations, pH 8. c) Normalized streaming current for different KCl concentrations, pH 8, for three nanopores ranging from 9 to 13 nm in diameter, and relative to their values at 0.1 M KCl. The dashed line represents the normalized current value reached at 0.1 M KCl. Six data points (at different transmembrane pressures) are collected during a pressure sweep, with 2–3 sweeps performed for each device tested, and the error bars indicate the 25% and 75% data quartiles respectively. The line and dot in the 50% quartile box represent the median and mean value respectively. d) Streaming current *versus* applied pressure gradient for a 9 nm nanopore in 0.1 M KCl at varying solution pH. e) Measured nanopore zeta potential in 0.1 M KCl at varying solution pH for ten nanopores ranging from 8 to 25 nm in diameter. Dashed line is a guide to the eye for the isoelectric point at ζ = 0 mV. f) Measured nanopore zeta potential for different KCl concentrations at pH 8 for three nanopores ranging from 9 to 13 nm in diameter. Error bars indicate the pooled standard deviation for these samples.

versus the ~10 nm ones is a significant factor that should be considered when performing these measurements, for which the noise and drift is often in the 1–10 pA range, and thus translates into a similar ~4-fold increase in the signal-to-noise ratio, facilitating the measurement.

The salt concentration of the surrounding fluid also influences the magnitude of the streaming current by governing the ion screening effects of the pore wall surface charge. Indeed, the extent of the screening effect (as characterized by the Debye length) is inversely proportional to the square root of the solution's salt concentration C as observed in eqn (3); a lower C thus leads to a longer λ and increases the extent of electrostatic interactions. Fig. 2(b) and (c) highlight how this property of the salt concentration affects the magnitude of the streaming current signal in a SiN nanopore. Fig. 2(b) plots the streaming current *versus* applied pressure gradient for varying KCl concentrations at pH 8 for a 9 nm diameter nanopore. At either end of the salt concentration sweep ranging from 0.01 M to 0.8 M, the magnitude of the streaming current is reduced (*e.g.* $<$ 1 pA for pressure gradients above 0.2 MPa in 0.01 M KCl) which we attribute to either the sparse number of ions available in the Stern layer at low salt concentration or by a greater screening of the surface at high salt concentrations (λ = 0.34 nm for 0.8 M KCl). Furthermore, when operating at >1 M KCl pH 8 (λ = 0.30 nm), these measurements become challenging to reproduce and interpret due to the finite sizes of the ions, both freely diffusing and in the adsorbed layer of counterions on the surface as described by the Stern model, when compared to Debye lengths in the single angstrom range. Fig. 2(c) plots the streaming current measurements of multiple pores (diameters 9–13 nm) over a salt concentration sweep, normalized by their values at 0.1 M KCl pH 8. It shows that, on average, the maximum signal-to-noise ratio is reached near this intermediate value ~0.1 M, with an asymptotic ~25% decrease in magnitude for ≥0.25 M KCl with these 20 nm thick nanopores. A similar, non-monotonic trend has been observed previously in silica nanochannels and was found to agree with chemical equilibrium models.[15]

Fig. 2(f) presents the measured variation in zeta potential over a sweep of bulk salt concentration. The zeta potential is

measured from 0.01 M to 0.8 M KCl, pH 8, and exhibits an analogous trend to the streaming current, with the highest surface potential recorded at 0.1 M KCl (−6.7 mV compared to −2.73 mV at 0.01 M and −5.45 mV at 0.8 M). Firnkes *et al.*[42] reported a monotonically decreasing surface potential magnitude in 0.1–0.4 M KCl, which is consistent with our results in that range. Meanwhile, calculated values of surface charge density ranged from −1.2 mC m^{-2} to −12.0 mC m^{-2} for bulk KCl concentrations between 0.01 M and 0.8 M at pH 8 (see Fig. S2 of the SI). Note from eqn (2) that the surface charge density is, to first order, proportional to the zeta potential, while being inversely proportional to the Debye length or the square root of the bulk concentration. These calculated surface charge density values, which follow a power law (with saturation at lower concentrations due to the challenge in extracting the streaming current explained earlier), qualitatively illustrate the differing rates of change between the zeta potential and the Debye length in varying KCl concentration.

We note, however, that these calculated surface charge densities, based on ζ values extracted under the streaming current method, should be considered as approximations, as they are known to deviate greatly from those of more direct (*e.g.* charge titration) measurements.[43] Furthermore, the assumptions that underline the simplified streaming current model (eqn (1)), from which our surface charge density estimates are derived, will not strictly hold as the zeta potential tends towards or exceeds the Debye–Huckel limit of ~25 mV. The surface charge density estimates can also be compared to values extracted from the conductance model of the nanopore:[44]

$$G = \frac{\pi d^2}{4L}\left[\left(\mu_K + \mu_{Cl}\right) n_{KCl} e + \mu_K \frac{4\sigma}{d}\right] \quad (4)$$

where μ_K, μ_{Cl}, n_{KCl} are the electrophoretic mobility of potassium and chloride ions, and the number density of potassium chloride ions, respectively (using values of μ_K = 7.616 × 10^{-8} m^2 V s^{-1} and μ_{Cl} = 7.909 × 10^{-8} m^2 V s^{-1}). Sections 3 and 4 of the SI present a detailed comparison of surface charge densities extracted from both measurement techniques and hypothesize that the observed differences are related to the initial assumptions made for the streaming current method and the distance away from the wall at which the measurement is performed.

Waduge *et al.*[45] reported that at 0.4 M KCl in pH 7.8, TEM drilled pores have a zeta potential of −7.9 ± 1.6 mV as measured with the streaming potential technique. In previous streaming current measurements, we reported a zeta potential value of −7.4 ± 1 mV at 100 mM KCl in pH 8,[34] and our present experimental data reveals a value of −5.22 ± 1.2 mV for 0.5 M KCl in pH 8 (see Fig. 2(f)). Although our experimental data falls within the measurement error reported, potential explanations for the lower mean value observed could include differences in the silicon nitride stoichiometry, wafer to wafer variations, and surface cleanliness. We also note that pores were fabricated by CBD directly in KCl aqueous solution in the present work and thus streaming current measurements here probe a freshly exposed surface inside the nanopore. Conversely, with nanopores fabricated by TEM drilling, an additional step of piranha cleaning is required to facilitate wetting.[46] This step further modifies the surface by promoting the formation of an oxide layer on top of the native silicon nitride and so is expected to result in surfaces featuring higher degrees of silanol dissociation exposed to solution, and thus higher measured streaming currents and zeta potentials. The solution's pH also strongly influences the surface charge density of the SiN membrane, again through silanol group dissociation.[47] This is a well-established equilibrium equation for SiN in basic and acidic solutions:

$$SiOH \leftrightarrow SiO^- + H^+ \quad (5)$$

$$SiNH^{3+} \leftrightarrow SiNH_2 + H^+ \quad (6)$$

Depending on the pH, *i.e.*, the concentration of hydrogen ions [H$^+$] in the bulk solution, the magnitude of the streaming current signal is impacted at a fixed salt concentration. To quantify this effect, Fig. 2(d) plots the streaming current *versus* an applied pressure gradient for a 9 nm pore at 100 mM KCl with varying pH and shows that, starting from pH 8 ([H$^+$] = 10^{-8} M), a decrease in concentration of hydrogen ions to pH 12 ([H$^+$] = 10^{-12} M) leads to an increase in the slope of the streaming current response with applied pressure, resulting for example in current magnitudes of −3.6 pA and −8 pA at 0.3 MPa applied pressure for pH 8 and 12, respectively. Similarly, an increase in hydrogen ions concentration from 10^{-8} M to 10$^{-4.6}$ M (pH 4.6) in the bulk solution leads to a decrease in streaming current magnitude and slope. The sign of the slope is also reversed when crossing the isoelectric point of the SiN membrane, turning the surface from being negatively charged at pH 4.6 to being positively charged at pH 3, as exemplified by values measured at 0.3 MPa of +1.2 pA at pH 3 compared to −2.1 pA at pH 4.6. The change in polarity of the current directly corresponds to a change in charge polarity of the ions shielding the surface.

Fig. 2(e) presents measured ζ values over a pH sweep for different nanopores (N = 10) of diameters ranging from 8 nm to 25 nm at a fixed salt concentration of 100 mM KCl (zeta potential is observed to be independent of pore dimensions in this range, as discussed above). The zeta potential is measured at −7.5 ± 0.9 mV at pH 8 and increases in magnitude (becomes more negative) as the bulk solution pH is increased to reach −20.5 ± 2 mV at pH 12. Similarly, by decreasing the bulk solution pH, the zeta potential becomes more positive and reaches a value of +1.7 mV ± 0.3 at 100 mM pH 3 after crossing the isoelectric point. This trend can also be translated to an estimated surface charge density after factoring in the solution's Debye length *via* eqn (2). Indeed, in this 100 mM KCl solution, the surface charge density is calculated to be +1.2 mC m^{-2}, −5.0 mC m^{-2}, and −14.2 mC m^{-2} at pH 3, pH 8 and pH 12 respectively (see section 1 of the SI).

By fitting the collected pH data to a power law, the isoelectric point of our CBD-fabricated SiN nanopores can be determined by the intercept where the ζ- or σ-value is zero. As reported by Lin *et al.*,[36] the isoelectric point of SiN is expected to be in the pH range of 4–5, for pores made by CBD and TEM drilling. Meanwhile, Sheetz *et al.*[37] report a value of 4.3 for CBD fabricated pores, as determined by nanopore conductance measurements (compared to the streaming current method adopted here). By interpolating within our fitted data, we obtain a SiN isoelectric point of 4.4 ± 0.1 for CBD fabricated pores, which is in good agreement with the above values, irrespective of the choice of fabrication method. We note here that the pH value was assumed to be the one measured in the bulk, whereas previous studies with silica nanopores showed that the recorded pH near the nanopore wall can differ by up to one unit from this bulk value when inspected by fluorescent dyes on the nanopore wall.[48]

Together, these measurements serve as a reference for the surface characteristics of SiN nanopores in the reported conditions of bulk salt concentration and pH, as well as validate the capabilities of our developed system to characterize the surface of nanopores.

Characterization of anti-fouling polymer coated nanopores through pore conductance, noise and zeta potential

Having optimized the conditions for surface potential characterization on bare SiN nanopores, we next explored providing an antifouling property to the nanopore surface or the surrounding membrane in order to improve sensing performance and investigate the mechanisms behind nanopore clogging. Functionalizing the nanopore surface can minimize surface interactions between the translocating analyte and the pore and thus reduce clogging artifacts, which are major limitations for long-duration biosensing, especially for samples with complex background mixtures[49] or certain biomolecules particularly prone to pore fouling like amyloid-alpha.[26] Here, we propose a protocol based on silane chemistry to preferentially functionalize the membrane surface and/or the pore interior. This protocol utilizes PAcrAm-*g*-PMOXA (SuSoS AG), as previously described by Awasthi *et al.*[50] for coating SiN nanopores. While this polymer has demonstrated potential in extending sensing time for protein detection through helium-ion-milling (HIM)-drilled pores, its application to nanopores fabricated by CBD has not been previously reported.

In particular, the CBD fabrication method facilitates the selective functionalization of the membrane and/or of the nanopore interior since the pore is formed *in situ*, *i.e.* directly in solution, with this technique. The membrane coating can thus be applied prior to pore formation and avoid being exposed to the potentially damaging vacuum and irradiation conditions encountered in energetic beam drilling fabrication methods.[46] CBD fabrication therefore readily facilitates three distinct coating scenarios: (1) coating the membrane surface before nanopore fabrication, resulting in a pristine, unmodified pore interior and functionalized membrane; (2) simultaneous functionalization of the membrane and nanopore interior post-fabrication; or (3) initial chemical modification of the membrane followed by incubation with a different coating post-nanopore fabrication, leading to distinct coatings inside and outside the pore.

Fig. 3(a) and (b) showcase two such coating strategies explored in this work using the PAcrAm-*g*-PMOXA polymer that targets the membrane surface and/or the pore interior. A cleaned SiN chip is mounted inside a flow cell, allowing for a sequence of solutions to be flushed onto the membrane surface to achieve functionalization, as well as providing electrical access to the membrane for a selectively placed step of nanopore fabrication by CBD in the protocol.

When the pore interior is coated, covalent bonding between the native silicon oxide sites on the SiN surface and the polymer's hydroxy (–OH) groups results in a neutrally charged interface of polymer extension (acryl–amide) groups, as seen by the analyte in solution.

One metric to characterize the functionalization of the pore interior is by measuring the open pore conductance, which should be predictably reduced after narrowing the pore diameter by the thickness of the polymer coating. The pore's DC conductance was determined by performing a current–voltage (I–V) measurement from −200 mV to +200 mV in 3.6 M LiCl at pH 8. Fig. 3(c) plots such I–V traces for two separate pores both before and after interior coating (Fig. 3(a)), leading to estimates of their pore diameters through a conductance model for cylindrical pore geometries.[51] As the polymer layer is expected to be approximately 1.5 nm thick,[52] the observed *ca.* ≃3 nm decrease in nanopore size after carrying out the coating protocol is consistent with having the pore interior fully coated.

Another means of characterizing the effect of antifouling coatings is by using power spectral density (PSD) measurements of the ionic current signal through the pore.[50] Fig. 3(d) compares the PSDs of a membrane-only coated chip and a bare SiN chip (3.6 M LiCl pH 8, Axopatch 200B, 100 kHz hardware filter), and both are observed to display similar $1/f$ noise performance at ±200 mV (both nanopores were ∼11 nm in diameter). Compared to previous nanopore functionalization strategies which involve coating the pore interior,[27,50] coating the membrane prior to pore fabrication eliminates the challenge of maintaining acceptable low frequency noise performance after functionalization, which has been a factor limiting the widespread use of surface coatings to reduce clogs. Fig. 3(e) highlights this phenomenon by plotting PSDs of a single pore (18 nm) both before and after interior coating with the antifouling polymer, with the post-coating PSD observed to feature a noticeable $1/f$ noise increase. Such an increase in low frequency noise when a pore is coated after fabrication (∼100× at 1 Hz) corresponds to pores with less stable open pore baselines, leading to molecular signals with reduced SNR and making molecular sensing challenging.

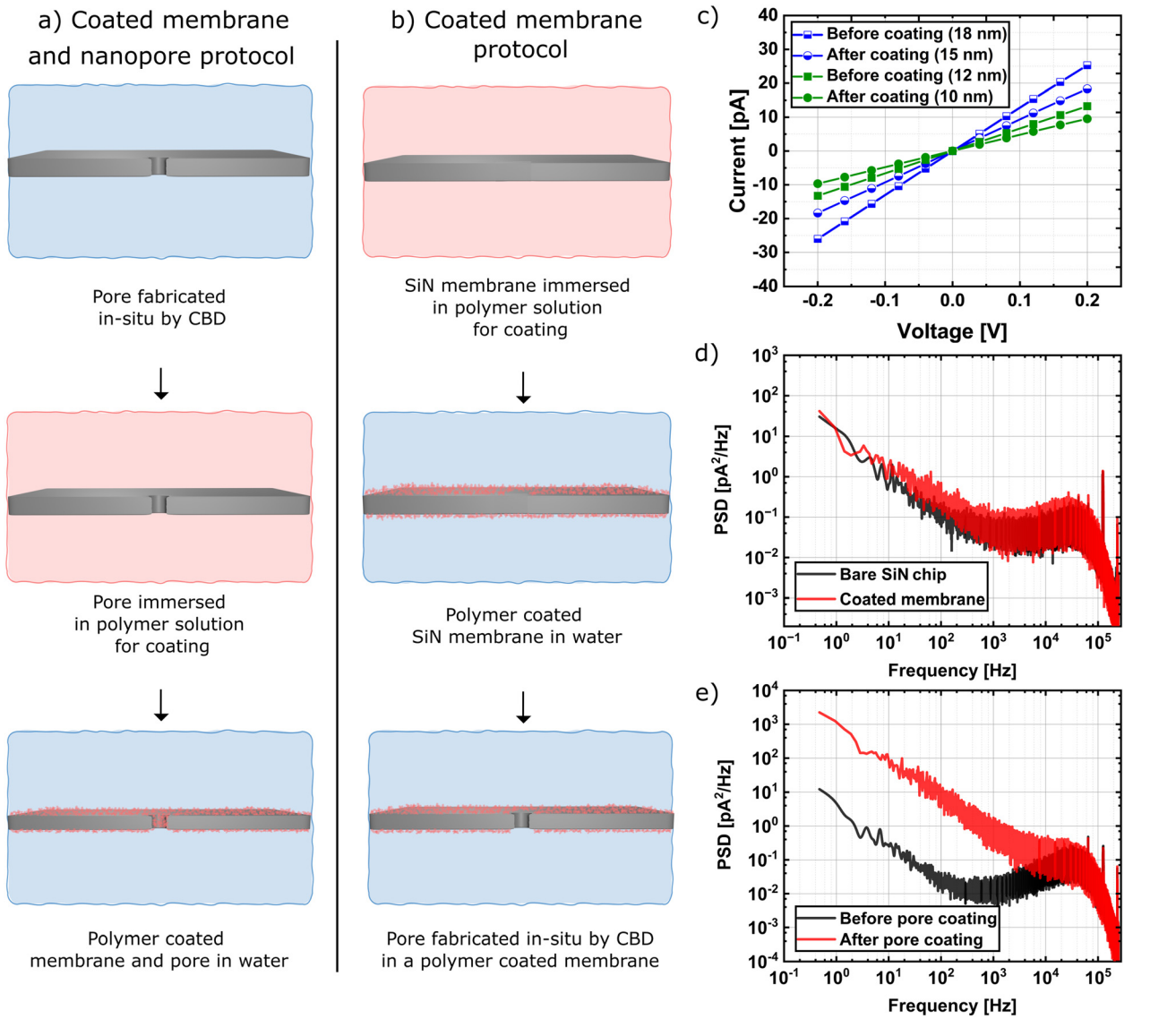

Fig. 3 Schematic of functionalization protocol for preferential *in situ* coating of SiN membranes and/or the pore interior and characterization through conductance and noise measurements. a) Protocol for coated membrane and pore interior: initial nanopore fabrication, incubation in 0.1 mg L^{-1} PAcrAm–PMOXA solution for 45 minutes, and DI water rinse before injecting the sensing solution with the sample of interest. b) Protocol for coated membrane: incubation in 0.1 mg mL^{-1} PAcrAm–PMOXA solution for 45 minutes, DI water rinse before CBD nanopore fabrication, then injection of sensing solution with the sample of interest. c) *I–V* curves for two nanopores (in blue and green) before and after interior surface coating. Estimated size is extracted from the slope of the data using a conductance model that assumes a cylindrical pore geometry.[51] d) Current power spectral density for a bare 11 nm SiN membrane device compared to an 11 nm nanopore device with its outer membrane surface coated (Axopatch 200B, 100 kHz hardware low pass filter). e) Current power spectral density for an initially 18 nm bare SiN device before and after coating of its inner pore surface (Axopatch 200B, 100 kHz hardware low pass filter).

Finally, we investigated the zeta potential, as measured by streaming current, as a key metric for probing the nanopore interior after surface modification.[53] Fig. 4(a) shows how the zeta potential across a pH range of 3 to 12 changes for the different types of devices tested, namely bare SiN membranes, coated membranes, and coated pore interiors, all immersed in a salt concentration of 100 mM KCl. As expected, the membrane coated devices, for which the pore interior remains a pristine SiN surface, exhibited similar zeta potential values to the bare SiN membrane devices across all tested pHs. Meanwhile, starting from pH 3, we observed a zeta potential of 0.9 ± 0.1 mV for fully coated nanopore devices compared to 2.0 ± 0.5 mV and 1.8 ± 0.4 mV for membrane coated and bare SiN pores respectively, representing a 50% decrease in the measured zeta potential between the bare SiN and fully coated nanopores. A similar behavior is exhibited between bare SiN and fully coated pores at pH 8, with a 56% decrease from −7.5 ± 1 mV to −3.3 ± 0.2 mV, and at pH 12, with a 72% decrease from −22.5 ± 3.8 mV to −6.3 ± 0.9 mV. Unlike polymer coatings with engineered end groups that react to solution pH,[25] the graft copolymer tested in this work is observed to passivate the surface with

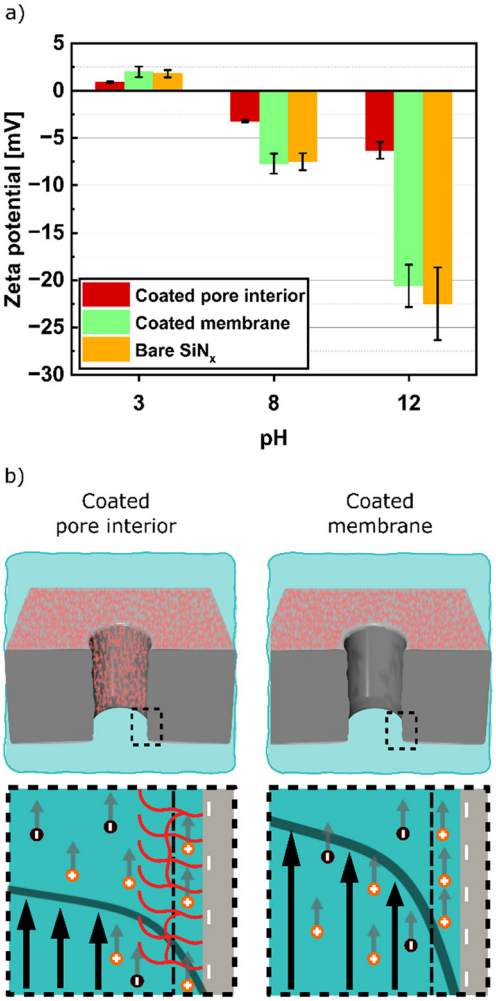

Fig. 4 Surface characteristics of functionalized nanopores. a) Measured zeta potential as a function of pH for the different devices tested (bare SiN membrane N = 10, coated membrane N = 2, and coated pore devices N = 2). Six data points (at different transmembrane pressures) are collected during a pressure sweep, leading to six zeta potential data points per sweep, with 2–3 sweeps performed for each device tested. Data points are then averaged, with a calculated standard deviation for each device at each pH value, and the error bars indicate the pooled standard deviation from all devices sharing a common pH and coating type. b) Schematic of the nanopore streaming current for devices under both coating protocols, illustrating the impact of the charge interface at the pore wall on the bulk solution flow.

an associated reduction in magnitude of the measured zeta potential, avoiding a complete polarity inversion of the surface charge density at a given pH.

The observed reduction in zeta potential is attributed to the covalent bonding of the polymer on the surface, which decreases liquid flow inside the channel due to the rigidity and density of these extended structures (Fig. 4(b)). Another possible explanation could be derived from the surface dissociation reactions (eqn (5) and (6)). As polymer adhesion to the surface increases, there is a reduction in free dissociated silanol groups, leading to fewer reaction sites at the interface between ions in the Debye layer and the surface. Consequently, this would result in decreased accumulation of counterions, and ultimately a reduced streaming current (and thus zeta potential or calculated surface charge density) being measured for polymer-coated nanopores.

Impact of nanopore functionalization on ssDNA translocation

Finally, in addition to surface characterization measurements, we investigated the changes in translocation characteristics associated with the surface functionalization. Specifically, we explored the anti-clogging properties of the two different strategies by recording the translocation of a linearized 7 knt long ssDNA genome from the M13 phage. This analyte is commonly used as the scaffold for DNA origami nanostructure assemblies and has previously shown a high propensity for clogging bare SiN solid-state nanopores.[23] Fig. 5 summarizes nanopore sensing experiments of M13 ssDNA in both bare and polymer-coated SiN membranes. In a bare 11 nm SiN nanopore, running a 5 nM M13 sample led to a clog event in less than 15 seconds, following 7 translocations (Fig. 5(a)). In contrast, nanopores featuring an outer membrane coating, with their inner pore surfaces either also coated or left bare, exhibited a significant increase in event counts and sensing durations. Fig. 5(b) shows the current trace at the start and end of an M13 ssDNA translocation experiment through an 11-nm pore coated only on its outer membrane surface. This pore recorded 3560 translocations of 7 knt long ssDNA M13 over the course of 45 minutes before permanently clogging. Section 5 of the SI additionally shows data for a 14-nm pore coated on the outer membrane only, with 13 813 events in 3120 seconds of recording. Similarly, two coated-interior pores (10 and 15 nm) were observed to register 2795 and 10 169 translocations of 7 knt ssDNA over durations of 2680 and 3720 seconds, respectively, before clogging (see section 5 of the SI). These results suggest that nanopore clogging behaviors with extended polymers are primarily a membrane surface interaction issue, with the analyte sticking point occurring somewhere outside of the pore interior. This general picture is consistent with the fact that the electric field strength is expected to be much weaker outside the pore than within its inner volume, and so proportionately smaller electrophoretic forces will be available in these regions when attempting to successfully dislodge a molecular clog. Overall, these translocation experiments highlight the effectiveness of surface coatings in extending sensing durations from seconds to $\gtrsim$1 hour (from $<$10 to ~1000–10 000 events, which is statistically sufficient for most studies) and shine light on the mechanism of nanopore clogging, *i.e.* of an analyte pinned outside the pore on the membrane and not necessarily stuck on the pore wall itself as proposed by others,[17–20,33] a phenomenon which currently widely impacts the field. Previous studies of nanopore clogging involved fluorescence microscopy to track polymers and conditions of pore clogging, yet the spatiotemporal resolution (~0.1–1 μm, ~1 ms) of these measurements makes it difficult

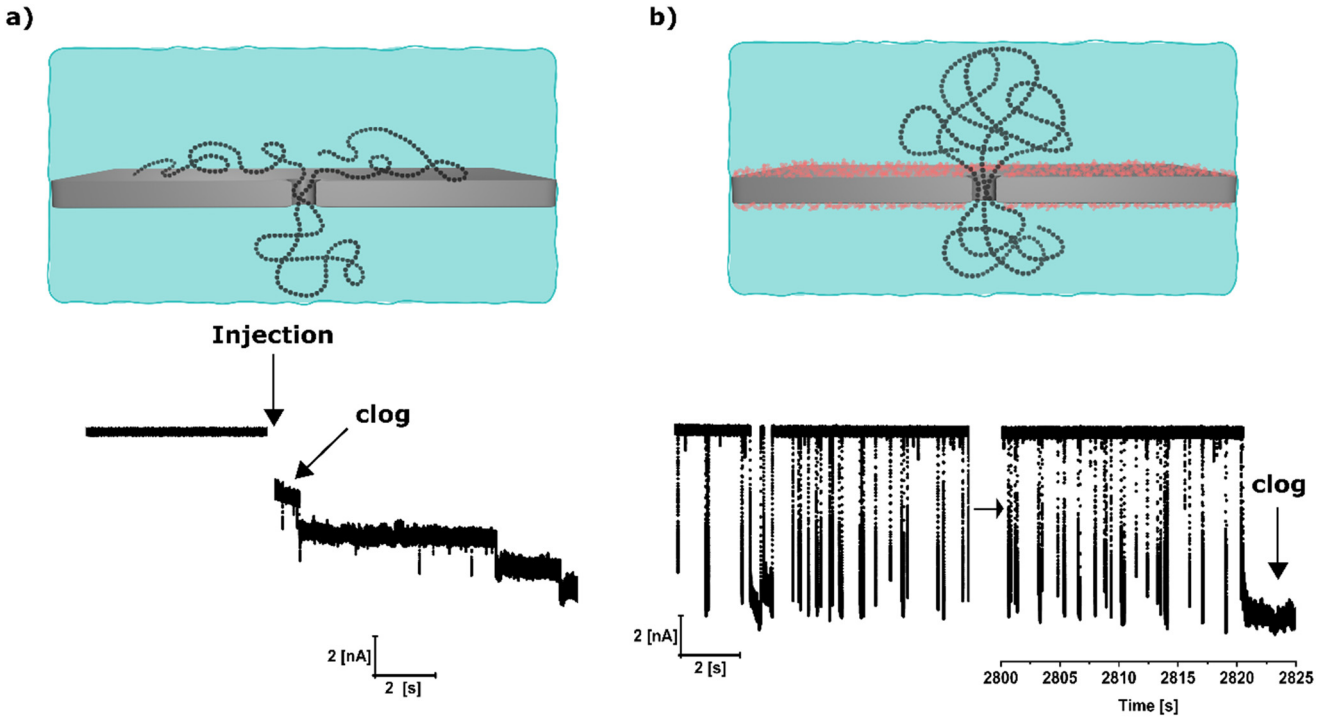

Fig. 5 Characterization of functionalized SiN nanopores for enhanced sensing duration of ssDNA (M13 scaffold, 7 knt). a) Schematic of ssDNA translocating through a bare SiN nanopore device (top) and ionic current traces (200 mV, 3.6 M LiCl) of a bare nanopore (11 nm) before and after ssDNA sample injection (bottom). b) Schematic of ssDNA translocating through a coated-membrane SiN nanopore device, demonstrating its anti-fouling capabilities (top), and ionic current traces (200 mV, 3.6 M LiCl) of a coated-membrane nanopore for the initial 15 seconds post ssDNA sample injection and, later, directly preceding an irreversible clogging event, demonstrating a ~45 minute increase in sensing time after functionalization (bottom).

to elucidate where the polymer is pinned relative to the nanometer dimensions of the pore. Furthermore, fluorescent dye labelling of DNA is known to alter its physical properties,[54] potentially increasing the likelihood of clogging, contrary to our present, label-free investigation of the clogging mechanism.

Building on these observations, Fig. 6(a) and (b) present scatter plots of maximum current blockage *versus* dwell time for the translocation events of two of the aforementioned coated pores, together representing both types of coating strategy. The smaller diameter nanopore (11 nm), with only its outer membrane coated, exhibited notably longer and more widely varying dwell times when passing M13 ssDNA (with a most probable duration, τ_{peak}, of ~10 000 μs, see Fig. 6(a)) compared to a 2 kbp dsDNA control molecule (τ_{peak} ≈ 100 μs). In contrast, the larger nanopore (15 nm), with its coated inner walls, exhibited shorter, narrowly distributed M13 ssDNA dwell times (τ_{peak} ≈ 126 μs, seen in Fig. 6(b)). This reduction in dwell time could possibly result from the presence of the polymer coating, which should act to shield the interior walls of the nanopore from interacting with the translocating sample, as well as to reduce the strength of electroosmotic flow opposing the electrophoretic transport of negative analytes, due to the lower effective surface charge (as characterized by zeta potential in the previous section). To further investigate this behavior, Fig. S6 presents a scatter plot of max current blockage *versus* dwell time for a 10 nm pore with coated inner walls and 14 nm pore with outer membrane coating. The observed dwell time increase with pore narrowing was found to still hold independently of the coating type, leading us to conclude that this particular dwell time variation is independent of the coating location, but is rather related to the pore diameter. It is interesting to note that the observed blockages for this 7 knt ssDNA are much deeper than the blockage of dsDNA, with both pores showing a comparable mean blockage of ΔI_{peak} ≈ 8–9 nA. This value is *ca.* 14-fold deeper than the measured single-file passage of dsDNA which resulted in blockages of ΔI_{peak} = 0.6 nA. This agrees with the previous observations of Kowalczyk *et al.*[55] that revealed that ssDNA and dsDNA are easily discriminated by their current blockages, with a reported conductance blockage level at 2 nS for 7 kb dsDNA compared to ~6–15 nS for 3.7 knt ssDNA in 1 M KCl pH 8. This implies that the ssDNA translocates in a stretched blob configuration (many segments in the pore at the same time) and not a linearized chain, as, given the highly flexible nature of the ssDNA, the tension front does not fully propagate along the contour length of the polymer.[56]

Conclusions

In this study, we presented an improved platform for performing low noise streaming current measurements through nanopores in order to characterize the pore surface potential and associated surface charge density. Our developed voltage-

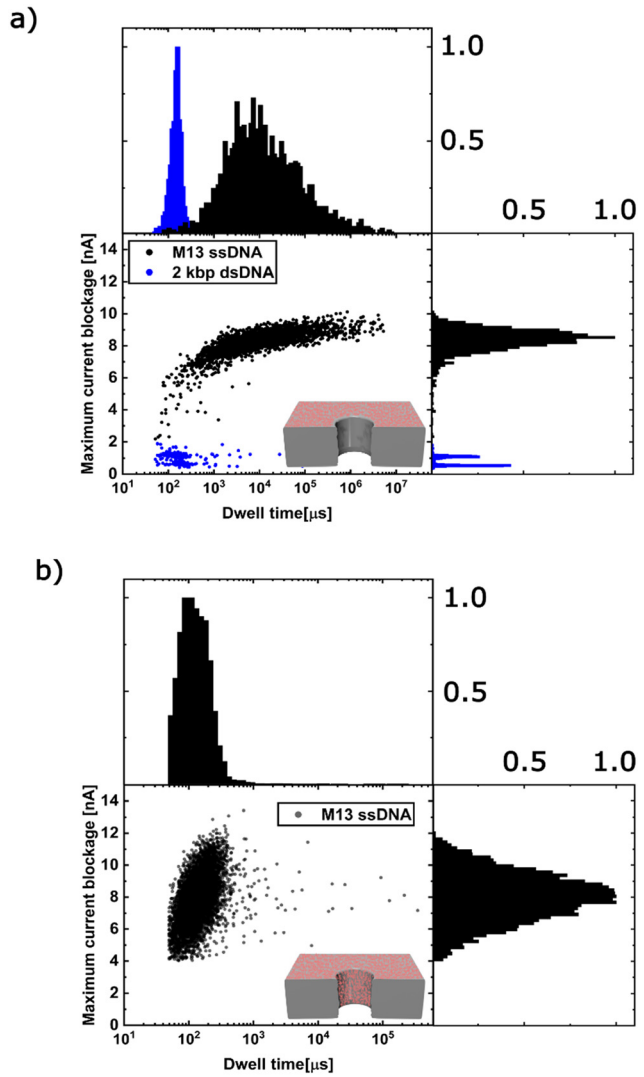

Fig. 6 DNA translocation characteristics in functionalized nanopores in 3.6 M LiCl pH 8, 200 mV, sampled at 500 kHz and digitally low-pass filtered (8-pole Bessel) at 100 kHz. a) Scatter plot of maximum ionic blockage *versus* passage time for M13 7 knt ssDNA and 2 kbp dsDNA translocation events (N = 3560) for an 11 nm nanopore with its outer membrane coated with an antifouling polymer. b) Scatter plot of M13 7 knt ssDNA translocation events (N = 10 169) for a 15 nm nanopore with its supporting membrane and interior wall coated.

and pressure-controlled setup enables high-pressure streaming current measurements in the 1–10 picoampere range with stable baselines. This allowed us to investigate the impact of pore size, salt concentration, and pH on the measured streaming current, and the trends of zeta potential and surface charge density with these parameters.

The streaming current platform was then used to characterize the surface of nanopores functionalized with an antifouling polymer coating. By adopting two different protocols tailored to preferentially target the outer membrane surface and/or the pore interior, we shed some light onto the mechanisms of nanopore clogging. To validate the effectiveness of the antifouling coating for extending the sensor lifetime, we translocated M13 DNA, a flexible 7 knt ssDNA genome that tends to otherwise instantly clog most bare SiN pores. Our findings point to one mechanism for "clog events" being associated with extended analytes irreversibly sticking to somewhere on the outer membrane surface near the pore (close enough for an end of the molecule to be captured), rather than within its interior volume as previously proposed.[17–20] By implementing spatially selective functionalization of the device, we addressed a key issue that has so far limited the widespread use of surface coatings to minimize pore clogging, namely adding antifouling functionality to pores without increasing the low-frequency noise of their ionic current signals. This greatly increases the usefulness of such pores for biosensing, thus paving the way for longer duration applications, including nanostructured DNA molecules for biomarker detection[49,57] and emerging protein sensing schemes.[58]

Experimental

Reagents

Potassium chloride (KCl), potassium hydroxide (KOH), lithium chloride (LiCl), lithium hydroxide (LiOH), hydrochloric acid (HCl), and HEPES (*N*-(2-hydroxyethyl)-piperazine-*N*′-(2 ethanesulfonic acid) buffer were purchased from Sigma-Aldrich. All solutions used in this study are prepared with ultrapure deionized water (18.2 MΩ cm at 25 °C) from a Milli-Q system. Conductivities of all prepared solutions were measured using a conductivity meter (Thermo Fisher Scientific, 018020MD). Solutions of 0.01 M, 0.1 M, 0.25 M, 0.5 M, 0.8 M KCl were diluted from a stock solution of 1 M KCl buffered with 10 mM HEPES at pH 8. Solutions of 0.1 M KCl at pHs of 3, 4.6, 8, 12 were prepared by dropwise titration of HCl or KOH into a master solution of 0.1 M KCl, pH 8 while using a pH meter (SB80PC VWR, 89231-580).

Pressure actuation and sensing

Mechanical pressure regulators were adopted in this study for a pressure actuation range of 0–0.3 MPa (SMC, IR2010-N02-R). Pressure sensing was based on a flow-through pressure sensor (MPS3, Elveflow), providing a voltage reading of 5–10 V that directly translates to a pressure reading using a calibration curve (a 5 V offset with a linear conversion of 10 PSI/V was taken from the sensor datasheet).

DNA samples

Linear dsDNA fragments of 2000 base pairs were purchased from Thermo Fisher (NoLimits, SM1701) as our calibration sample. Flexible ssDNA samples were purchased from Tilibit Nanosystems (M13mp18, type p7249). Both samples were mixed with 3.6 M LiCl buffered with 10 mM HEPES at pH 8 to reach a sample concentration of 5 nM in an 80 μL volume.

Salt bridge

Photo initiator Irgacure or 2-hydroxy-4′-(2-hydroxyethoxy)-2 methylpropiophenone (Sigma-Aldrich, 410896) was first

dissolved in 99% (wt/wt) ethanol (VWR, 200004-488) at a concentration of 10% (w/v), then mixed with pure PEGDa (Sigma-Aldrich, 437441) and 3 M KCl pH 8, reaching a final PEGDa concentration of 40% (v/v) with a 1% (w/v) photo initiator concentration. This mixture was introduced in ~20 mm long PTFE tubes with an external diameter of 1/32″ (Cole Parmer) using a low vacuum setup, then exposed to UV light in the 450 nm range until cured. Finally, Ag/AgCl electrodes were submersed in a vial filled with 3 M KCl electrolyte and connected to a separate sensing vial (containing an electrolyte of variable salt concentration and pH, see Fig. 1) through the developed PEGDa-filled tubing. This provided an electrical connection between the two vials (≲10 kΩ access resistance) while decoupling the direct exposure of the electrode to the sensing solution, thus reducing electrode drift during sensing as well as degradation over time.

Surface coating

PAcrAm-*g*-PMOXA (poly(acryl-amide)-*g*-(PMOXA$_{50}$, 1,6-hexanediamine, 3-aminopropyldimethylsilanol)) was obtained from SuSoS AG, Switzerland. The dried sample was dissolved to a concentration of 1 mg mL^{-1} in ultrapure water (18.2 MΩ cm) containing 10 mM HEPES buffer (pH 7.4), then diluted 10 times to reach a polymer concentration of 0.1 mg mL^{-1}. Chips were Piranha cleaned (3 : 1 H_2SO_4 and 30% H_2O_2) for 1 hour at 90 °C, followed by a DI water rinse before moving to an RCA1 clean (5 : 1 : 1 DI water, NH_4OH, and 30% H_2O_2) for 15 minutes at 80 °C, then dried using N_2. After mounting in a flow cell, one of two coating protocols is followed (see Fig. 3). For outer membrane surface and pore interior coating, the CBD protocol is first performed in 1 M KCl solution to create a nanopore of the desired size (factoring in an assumed ~3 nm reduction in diameter after the later coating step). After a DI water flush, the polymer coating is introduced into the flow cell at a 0.1 mg mL^{-1} concentration and incubated for 45 minutes for optimal results. A second DI water flush is required before finally adding the sensing solution for streaming current or DNA translocation experiments. For outer membrane coating only, the 0.1 mg mL^{-1} polymer solution is directly injected into the flow cell after mounting the chip containing an intact membrane and is again incubated for 45 minutes. DI water is then flushed to rinse out excess coating polymer and the subsequent CBD pore fabrication step is performed. This results in a nanopore of the desired size featuring bare inner walls and coated outer membrane.

Nanopore sensing

All nanopores used in this work were made on 5 mm square chips featuring 60 × 60 μm^2 free-standing membranes of 20 nm thin SiN, deposited at Addison Semiconductor Materials, Inc (Low stress LPCVD Nitride, film tensile stress <250 ± 50 MPa) and manufactured in-house at the uOttawa NanoFab facilities. Ionic current sensing was carried out on a single-channel patch-clamp amplifier (Axopatch 200B, Molecular Devices). An acquisition card (NI USB-6353, National Instruments) was used to interface between the amplifier, the pressure sensor, and the computer.

Signal processing

Streaming current data was processed from the acquisition card and software low-pass filtered (8-pole Bessel) at 10 Hz. This data processing was performed using a custom Python script. DNA translocation data was sampled at a rate of 500 kHz and software low-pass filtered (8-pole Bessel) at 100 kHz. An in-house implementation of the CUSUM+ algorithm is used to extract relevant information from recorded current traces (Nanolyzer, Northern Nanopore Instruments).[59]

Conflicts of interest

All authors declare no conflict of interest.

Abbreviations

CBD	Controlled breakdown
EDL	Electrical double layer
PEG	Polyethylene glycol
ssDNA	Single-stranded DNA
dsDNA	Double-stranded DNA
TEM	Transmission electron microscopy
knt	Kilo nucleotides

Data availability

Data presented in the figures is added as an Excel document (Fig. 1c, 2, 4a, 6 and S1–S4). See DOI: **https://doi.org/10.1039/D5LF00147A**.

The data supporting this article have been included in the SI.

Acknowledgements

The authors would like to the acknowledge the support of the Natural Sciences and Engineering Research Council of Canada (NSERC) [funding reference number RGPIN-2021-04304, I2IPJ 586238-23], and Oxford Nanopore Technologies. MYB would like to thank Dr. Shan Zou (National Research Council Canada) for fruitful discussions. We also thank Dmytro Lomovtsev, Gengyang Mu, Matthew Waugh, and Martin Charron for many training sessions around flow cell design, device microfabrication and insightful discussions about streaming current concepts.

References

1 J. A. Alfaro, P. Bohländer, M. Dai, M. Filius, C. J. Howard and X. F. Van Kooten, *et al.*, The emerging landscape of single-molecule protein sequencing technologies, *Nat. Methods*, 2021, **18**(6), 604–617.

2 Y. L. Ying, Z. L. Hu, S. Zhang, Y. Qing, A. Fragasso and G. Maglia, *et al.*, Nanopore-based technologies beyond DNA sequencing, *Nat. Nanotechnol.*, 2022, **17**(11), 1136–1146.

3 A. Dorey and S. Howorka, Nanopore DNA sequencing technologies and their applications towards single-molecule proteomics, *Nat. Chem.*, 2024, **16**(3), 314–334.
4 L. Xue, H. Yamazaki, R. Ren, M. Wanunu, A. P. Ivanov and J. B. Edel, Solid-state nanopore sensors, *Nat. Rev. Mater.*, 2020, **5**(12), 931–951.
5 H. Kwok, K. Briggs and V. Tabard-Cossa, Nanopore fabrication by controlled dielectric breakdown, *PLoS One*, 2014, **9**(3), e92880.
6 M. Waugh, K. Briggs, D. Gunn, M. Gibeault, S. King and Q. Ingram, *et al.*, Solid-state nanopore fabrication by automated controlled breakdown, *Nat. Protoc.*, 2020, **15**(1), 122–143.
7 V. Tabard-Cossa, D. Trivedi, M. Wiggin, N. N. Jetha and A. Marziali, Noise analysis and reduction in solid-state nanopores, *Nanotechnology*, 2007, **18**(30), 305505.
8 R. M. M. Smeets, U. F. Keyser, N. H. Dekker and C. Dekker, Noise in solid-state nanopores, *Proc. Natl. Acad. Sci. U. S. A.*, 2008, **105**(2), 417–421.
9 V. Tabard-Cossa, Instrumentation for Low-Noise High-Bandwidth Nanopore Recording, *Engineered Nanopores for Bioanalytical Applications*, Elsevier, 2013, pp. 59–93.
10 A. Fragasso, S. Schmid and C. Dekker, Comparing Current Noise in Biological and Solid-State Nanopores, *ACS Nano*, 2020, **14**(2), 1338–1349.
11 R. M. M. Smeets, U. F. Keyser, M. Y. Wu, N. H. Dekker and C. Dekker, Nanobubbles in Solid-State Nanopores, *Phys. Rev. Lett.*, 2006, **97**(8), 088101.
12 A. Fragasso, S. Pud and C. Dekker, $1/f$ noise in solid-state nanopores is governed by access and surface regions, *Nanotechnology*, 2019, **30**(39), 395202.
13 J. Saharia, Y. M. N. D. Y. Bandara, B. I. Karawdeniya, G. Alexandrakis and M. J. Kim, Assessment of $1/f$ noise associated with nanopores fabricated through chemically tuned controlled dielectric breakdown, *Electrophoresis*, 2021, **42**(7–8), 899–909.
14 D. P. Hoogerheide, S. Garaj and J. A. Golovchenko, Probing Surface Charge Fluctuations with Solid-State Nanopores, *Phys. Rev. Lett.*, 2009, **102**(25), 256804.
15 F. H. J. Van Der Heyden, D. Stein and C. Dekker, Streaming Currents in a Single Nanofluidic Channel, *Phys. Rev. Lett.*, 2005, **95**(11), 116104.
16 K. Lin, Z. Li, Y. Tao, K. Li, H. Yang and J. Ma, *et al.*, Surface Charge Density Inside a Silicon Nitride Nanopore, *Langmuir*, 2021, **37**(35), 10521–10528.
17 G. Ando, C. Hyun, J. Li and T. Mitsui, Directly Observing the Motion of DNA Molecules near Solid-State Nanopores, *ACS Nano*, 2012, **6**(11), 10090–10097.
18 T. Kubota, K. Lloyd, N. Sakashita, S. Minato, K. Ishida and T. Mitsui, Clog and Release, and Reverse Motions of DNA in a Nanopore, *Polymer*, 2019, **11**(1), 84.
19 S. Li, S. Zeng, C. Wen, L. Barbe, M. Tenje and Z. Zhang, *et al.*, Dynamics of DNA Clogging in Hafnium Oxide Nanopores, *J. Phys. Chem. B*, 2020, **124**(51), 11573–11583.
20 O. M. Eggenberger, C. Ying and M. Mayer, Surface coatings for solid-state nanopores, *Nanoscale*, 2019, **11**(42), 19636–19657.
21 A. Frutiger, A. Tanno, S. Hwu, R. F. Tiefenauer, J. Vörös and N. Nakatsuka, Nonspecific Binding—Fundamental Concepts and Consequences for Biosensing Applications, *Chem. Rev.*, 2021, **121**(13), 8095–8160.
22 M. Wanunu and A. Meller, Chemically Modified Solid-State Nanopores, *Nano Lett.*, 2007, **7**(6), 1580–1585.
23 Z. Tang, B. Lu, Q. Zhao, J. Wang, K. Luo and D. Yu, Surface Modification of Solid-State Nanopores for Sticky-Free Translocation of Single-Stranded DNA, *Small*, 2014, **10**(21), 4332–4339.
24 J. Andersson, J. Järlebark, S. Kk, A. Schaefer, R. Hailes and C. Palasingh, *et al.*, Polymer Brushes on Silica Nanostructures Prepared by Aminopropylsilatrane Click Chemistry: Superior Antifouling and Biofunctionality, *ACS Appl. Mater. Interfaces*, 2023, **15**(7), 10228–10239.
25 Y. M. Nuwan D. Y. Bandara, B. I. Karawdeniya, J. T. Hagan, R. B. Chevalier and J. R. Dwyer, Chemically Functionalizing Controlled Dielectric Breakdown Silicon Nitride Nanopores by Direct Photohydrosilylation, *ACS Appl. Mater. Interfaces*, 2019, **11**(33), 30411–30420.
26 E. C. Yusko, J. M. Johnson, S. Majd, P. Prangkio, R. C. Rollings and J. Li, *et al.*, Controlling protein translocation through nanopores with bio-inspired fluid walls, *Nat. Nanotechnol.*, 2011, **6**(4), 253–260.
27 O. M. Eggenberger, G. Leriche, T. Koyanagi, C. Ying, J. Houghtaling and T. B. H. Schroeder, *et al.*, Fluid surface coatings for solid-state nanopores: comparison of phospholipid bilayers and archaea-inspired lipid monolayers, *Nanotechnology*, 2019, **30**(32), 325504.
28 Y. Dai, Y. Zhang, Q. Ma, M. Lin, X. Zhang and F. Xia, Inner Wall and Outer Surface Distinguished Solid-State Nanopores for Sensing, *Anal. Chem.*, 2022, **94**(50), 17343–17348.
29 A. Ivankin, R. Y. Henley, J. Larkin, S. Carson, M. L. Toscano and M. Wanunu, Label-Free Optical Detection of Biomolecular Translocation through Nanopore Arrays, *ACS Nano*, 2014, **8**(10), 10774–10781.
30 R. Wang, T. Gilboa, J. Song, D. Huttner, M. W. Grinstaff and A. Meller, Single-Molecule Discrimination of Labeled DNAs and Polypeptides Using Photoluminescent-Free TiO_2 Nanopores, *ACS Nano*, 2018, **12**(11), 11648–11656.
31 L. Chazot-Franguiadakis, J. Eid, M. Socol, B. Molcrette, P. Guégan and M. Mougel, *et al.*, Optical Quantification by Nanopores of Viruses, Extracellular Vesicles, and Nanoparticles, *Nano Lett.*, 2022, **22**(9), 3651–3658.
32 H. S. Varol, D. Kaya, E. Contini, C. Gualandi and D. Genovese, Fluorescence methods to probe mass transport and sensing in solid-state nanoporous membranes, *Mater. Adv.*, 2024, **5**(21), 8351–8383.
33 A. Egatz-Gomez, C. Wang, F. Klacsmann, Z. Pan, S. Marczak and Y. Wang, *et al.*, Future microfluidic and nanofluidic modular platforms for nucleic acid liquid biopsy in precision medicine, *Biomicrofluidics*, 2016, **10**(3), 032902.
34 M. Y. Bouhamidi, D. Lomovtsev, G. Mu, M. Charron, M. Waugh and V. Tabard-Cossa, Characterizing Surface Charge Density of Solid-State Nanopore Sensors for Improved Biosensing Applications, *2023 IEEE Sensors Applications Symposium (SAS)*, IEEE, Ottawa, ON, Canada, 2023, pp. 1–5.

35 T. Albrecht, T. Gibb and P. Nuttall, Ion Transport in Nanopores, *Engineered Nanopores for Bioanalytical Applications*, Elsevier, 2013, pp. 1–30.
36 C. Y. Lin, E. Turker Acar, J. W. Polster, K. Lin, J. P. Hsu and Z. S. Siwy, Modulation of Charge Density and Charge Polarity of Nanopore Wall by Salt Gradient and Voltage, *ACS Nano*, 2019, **13**(9), 9868–9879.
37 B. S. Sheetz and J. R. Dwyer, Probing nanopore surface chemistry through real-time measurements of nanopore conductance response to pH changes, *Rev. Sci. Instrum.*, 2023, **94**(10), 104101.
38 W. F. Wonderlin, A. Finkel and R. J. French, Optimizing planar lipid bilayer single-channel recordings for high resolution with rapid voltage steps, *Biophys. J.*, 1990, **58**(2), 289–297.
39 C. T. A. Wong and M. Muthukumar, Polymer translocation through α-hemolysin pore with tunable polymer-pore electrostatic interaction, *J. Chem. Phys.*, 2010, **133**(4), 045101.
40 B. J. Kirby and E. F. Hasselbrink Jr., Zeta potential of microfluidic substrates: 1. Theory, experimental techniques, and effects on separations, *Electrophoresis*, 2004, **25**(2), 187–202.
41 M. Mao, J. D. Sherwood and S. Ghosal, Electro-osmotic flow through a nanopore, *J. Fluid Mech.*, 2014, **749**, 167–183.
42 M. Firnkes, D. Pedone, J. Knezevic, M. Döblinger and U. Rant, Electrically Facilitated Translocations of Proteins through Silicon Nitride Nanopores: Conjoint and Competitive Action of Diffusion, Electrophoresis, and Electroosmosis, *Nano Lett.*, 2010, **10**(6), 2162–2167.
43 B. J. Kirby, *Micro- and Nanoscale Fluid Mechanics: Transport in Microfluidic Devices*, 1st edn, Cambridge University Press, 2012.
44 R. M. M. Smeets, U. F. Keyser, D. Krapf, M. Y. Wu, N. H. Dekker and C. Dekker, Salt Dependence of Ion Transport and DNA Translocation through Solid-State Nanopores, *Nano Lett.*, 2006, **6**(1), 89–95.
45 P. Waduge, R. Hu, P. Bandarkar, H. Yamazaki, B. Cressiot and Q. Zhao, *et al.*, Nanopore-Based Measurements of Protein Size, Fluctuations, and Conformational Changes, *ACS Nano*, 2017, **11**(6), 5706–5716.
46 *Nanostructure Science and Technology*, Solid State Nanopores: From Fabrication to Biosensing, ed. J. P. Leburton, Springer International Publishing, Cham, 2023.
47 H. J. Butt and M. Kappl, *Surface and Interfacial Forces 2e*, 1st edn, Wiley, 2018.
48 S. Schneider, M. Brodrecht, H. Breitzke, T. Wissel, G. Buntkowsky and H. S. Varol, *et al.*, Local and diffusive dynamics of LiCl aqueous solutions in pristine and modified silica nanopores, *J. Chem. Phys.*, 2022, **157**(3), 034503.
49 L. He, D. R. Tessier, K. Briggs, M. Tsangaris, M. Charron and E. M. McConnell, *et al.*, Digital immunoassay for biomarker concentration quantification using solid-state nanopores, *Nat. Commun.*, 2021, **12**(1), 5348.
50 S. Awasthi, P. Sriboonpeng, C. Ying, J. Houghtaling, I. Shorubalko and S. Marion, *et al.*, Polymer Coatings to Minimize Protein Adsorption in Solid-State Nanopores, *Small Methods*, 2020, **4**(11), 2000177.
51 S. W. Kowalczyk, A. Y. Grosberg, Y. Rabin and C. Dekker, Modeling the conductance and DNA blockade of solid-state nanopores, *Nanotechnology*, 2011, **22**(31), 315101.
52 A. S. Mertgen, A. G. Guex, S. Tosatti, G. Fortunato, R. M. Rossi and M. Rottmar, *et al.*, A low-fouling, self-assembled, graft co-polymer and covalent surface coating for controlled immobilization of biologically active moieties, *Appl. Surf. Sci.*, 2022, **584**, 152525.
53 R. Zimmermann, W. Norde, M. A. Cohen Stuart and C. Werner, Electrokinetic Characterization of Poly(Acrylic Acid) and Poly(Ethylene Oxide) Brushes in Aqueous Electrolyte Solutions, *Langmuir*, 2005, **21**(11), 5108–5114.
54 L. S. Lerman, Structural considerations in the interaction of DNA and acridines, *J. Mol. Biol.*, 1961, **3**(1), 18-IN14.
55 S. W. Kowalczyk, M. W. Tuijtel, S. P. Donkers and C. Dekker, Unraveling Single-Stranded DNA in a Solid-State Nanopore, *Nano Lett.*, 2010, **10**(4), 1414–1420.
56 P. Mensing, M. Charron, M. Y. Bouhamidi and V. Tabard-Cossa, Folding Dynamics of Linear ssDNA–dsDNA Heterostructures through Solid-State Nanopores, *Macromolecules*, 2025, **58**(8), 4094–4102.
57 J. Zhu, N. Ermann, K. Chen and U. F. Keyser, Image Encoding Using Multi-Level DNA Barcodes with Nanopore Readout, *Small*, 2021, **17**(28), 2100711.
58 S. Dutt, H. Shao, B. Karawdeniya, Y. M. Nuwan D. Y. Bandara, E. Daskalaki and H. Suominen, *et al.*, High Accuracy Protein Identification: Fusion of Solid-State Nanopore Sensing and Machine Learning, *Small Methods*, 2023, **7**(11), 2300676.
59 Z. Roelen, K. Briggs and V. Tabard-Cossa, Analysis of Nanopore Data: Classification Strategies for an Unbiased Curation of Single-Molecule Events from DNA Nanostructures, *ACS Sens.*, 2023, **8**(7), 2809–2823.